ISSN 0006-3509, Biophysics, 2017, Vol. 62, No. 5, pp. 778–795. © Pleiades Publishing, Inc., 2017.
Original Russian Text © E.L. Mishchenko, O.V. Petrovskaya, A.M. Mishchenko, E.D. Petrovskiy, N.V. Ivanisenko, V.A. Ivanisenko, 2017, published in Biofizika, 2017, Vol. 62, No. 5, pp. 949–968.

BIOPHYSICS OF COMPLEX SYSTEMS

Integrated Mathematical Models for Describing Complex Biological Processes

E. L. Mishchenko[a], *, O. V. Petrovskaya[a], A. M. Mishchenko[b], E. D. Petrovskiy[a], N. V. Ivanisenko[a], and V. A. Ivanisenko[a]

[a] *Institute of Cytology and Genetics, Siberian Branch, Russian Academy of Sciences, Novosibirsk, 630090 Russia*

[b] *Novosibirsk State University, Novosibirsk, 630090 Russia*

**e-mail: elmish@bionet.nsc.ru*

Received February 17, 2017

Abstract—This review describes integrated mathematical models of processes, such as calcium homeostasis, pathogen–host interaction (with hepatitis C virus as a pathogen), and the response of the human brain to a stimulating event. It is shown that integrated mathematical models provide a deeper insight into the mechanisms and conditions that lead to the development of diseases of different natures (musculoskeletal disorders, viral infections, and various impairments in brain function) and aid identification of the key targets and conditions for a directed effect of new generation drugs, as well as the interpretation of the results of state-of-the-art CT imaging.

Keywords: mathematical modeling, calcium homeostasis, hepatitis C virus, human brain, stimulating event, mechanisms of diseases, therapeutic effects

DOI: 10.1134/S0006350917050141

Research into the interactions in complex biological processes is one of the central challenges in systems biology and contributes to the insight into the mechanisms that underlie many diseases, their patterns, and course as well as to explanation of the effects of the used therapies [1–3]. In particular, intersection of the signaling pathways of the estrogen and growth factor receptors is one of the causes of tamoxifen resistance (tamoxifen is a selective modulator of the estrogen receptor and a well-known anticancer drug used for breast cancer treatment) [1]. The review by Javelaud and Mauviel [2] described the interaction of mitogen-activated protein kinase (MAPK) and the Smad signaling pathways, which are activated by transforming growth factor β (TGF-β). Individual MAPK and Smad pathways lead to activation of the transcription factors that regulate cell proliferation, differentiation, mobility, and apoptosis as well as tumorigenesis. The MAPK and Smad pathways intersect when the linker regions of Smad proteins are phosphorylated by MAP kinases; in many cases, this influences the ability of Smad proteins to translocate to the nucleus, where they are involved in formation of manifold heterogeneous transcription complexes. An indirect interaction of the MAPK and Smad pathways includes the expression control of some Smad proteins and their posttranslational modification by MAP kinases. In particular, the interaction of MAPK and Smad pathways has a strong effect on carcinogenesis by depleting the antiproliferative response, inhibiting apoptosis, enhancing tumor cell transdifferentiation into a highly aggressive metastatic phenotype, and accelerating bone spreading in breast and prostate cancers.

Another review [3] described the mechanism that underlies the function of the NF-κB family of transcription factors and their role in expression of over 100 genes, most of which are involved in the immune response, as well as in carcinogenesis, stress response, and regulation of apoptosis. The signaling pathways that activate NF-κB are an attractive target for viruses, which having infected a cell are able to induce cellular signals that activate these pathways. In addition, some viral proteins can directly interact with signaling molecules and stimulate NF-κB induction. In this case, the NF-κB activity can stimulate transcription not only of cellular genes, but also of viral genes in the virus-infected cells. In particular, NF-κB factor and

Abbreviations: MAPK, mitogen-activated protein kinase; TGF-β, transforming growth factor; HCV, hepatitis C virus; PTH, parathyroid hormone; RANK, receptor activator of nuclear factor NF-κB; RANKL, RANK ligand; OPG, osteoprotegerin; IFN-α, interferon α; fMRI, functional magnetic resonance imaging; MRS, magnetic resonance spectroscopy; BOLD signal, blood oxygen level–dependent signal; ANLS, astrocyte–neuron lactate shuttle.

the upstream multisubunit IKK (IκB kinase) complex of the signaling NF-κB pathway in the cell lines infected with human immunodeficiency virus (HIV-1) are constantly active. It is known that the HIV-1 promoter proximal (enhancer) region contains two adjacent NF-κB binding sites [3]; correspondingly, this transcription factor plays a key role in induction of the HIV-1 gene expression. This expression is additionally boosted by the Sp-1 transcription factor, which interacts with several sites adjacent to the NF-κB binding sites. Other viruses, for example, human T-cell leukemia virus (that causes acute T-cell leukemia), γ-herpes virus (that causes lymphoproliferative diseases and is associated with Kaposi sarcoma and multiple myeloma), and hepatitides B and C (which potentially lead to hepatocarcinoma development), also follow analogous strategies for stable activation of cellular NF-κB pathway to stimulate transcription of their genes. The strategies used by viruses for activation of the NF-κB pathway lead to an increase in virus replication, preserve the viability of infected cells, enhance their unlimited proliferation, and inhibit the immune response and apoptosis.

One of the approaches to studying the functioning of the gene networks that describe the interactions in complex biological processes is mathematical modeling. The major problem when constructing mathematical models is the knowledge of kinetic parameters; correspondingly, most of the currently existing models have been built for well-studied processes, such as cholesterol metabolism [4], influenza virus A infection [5], RNA replication of hepatitis C virus replicon [6], and inflammation development in rheumatoid arthritis [7]. Since complex processes are described via the interactions of gene networks, integrated models, describing the interactions both within individual gene networks and between networks in an integrated manner, have recently appeared. Construction of such integrated models requires that the common objects (common variables) involved in the interaction of gene networks or the interaction between different objects (different variables) of networks are known. Although data about direct interactions of gene networks is frequently absent in the literature, the indirect data on mutual effects of gene networks on one another is abundant. One example of such information is the changes in expression levels of all genes or part of them in a gene network in response to knockout or inhibition of a specific gene or group of genes in another gene network [8, 9]. A new approach has been recently proposed based on such experimental data that allows for integration of independent mathematical models of replication of hepatitis C virus subgenomic replicon in cells and apoptosis induction pathways via introduction of control functional [10].

This review describes some examples of integrated mathematical models that describe interactions in the intricate functioning systems, such as calcium homeostasis in the body, host–hepatitis C virus, and human brain–stimulatory event. Integrated models explain in a formalized form the dynamics of pathological processes in these systems, the mechanisms leading to disease progression, as well as clinical and therapeutic effects, while analysis of such models forms the background for development of new treatment strategies.

AN INTEGRATED MODEL OF CALCIUM HOMEOSTASIS AND BONE RECONSTRUCTION IN THE HUMAN BODY

The system of calcium homeostasis in the human body is extremely intricate and consists of hormones, most of which are known; the key players here are parathyroid hormone (PTH), calcitriol 1α,25-dihydroxyvitamin D_3), calcitonin, as well as the free calcium of the body's extracellular compartment. The parathyroid glands are a calcium-dependent endocrine organ, which instantly responds via its calcium-sensing receptors by an increase in PTH secretion to even the most insignificant decrease in intracellular calcium concentration. PTH fulfills several functions; namely, it activates D-1α-hydroxylase, the enzyme that hydroxylates 25-dihydroxyvitamin D_3 to give calcitriol in the kidneys; regulates the critical level of excretion of calcium and phosphate ions, and calcium exchange between bone tissue and extracellular fluid. Calcitriol inhibits its own synthesis, stimulates the absorption of Ca^{2+} and phosphate ions in the small intestine, and inhibits excretion of calcium and phosphate ions in the kidneys. In the presence of PTH, calcitriol regulates calcium exchange between the bone tissue and the extracellular compartment. In turn, calcium and calcitriol regulate PTH production in the parathyroid glands. The calcium excretion in the kidneys and its accumulation in the bone tissue are also regulated by free calcium and calcitonin [11]. Disturbance of the calcium homeostasis cause severe diseases, such as hypocalcemia and hypercalcemia, osteoporosis, and rachitis.

A minimal model [12] describes the dynamics of the key players and regulators of the systemic calcium homeostasis in the human body, including calcium and phosphate in the total bone and intercellular compartments, phosphate in the total cellular compartment, PTH in the intercellular compartment, 1α-hydroxylase in the kidneys, calcitriol in the intercellular compartment, calcium transporters in the intestine, and the pool of active cells that secrete PTH in the parathyroid glands. The model consists of 11 nonlinear differential equations that describe the dynamics of component x (calcium, phosphate, PTH, 1α-hydroxylase, calcitriol, calcium transport-

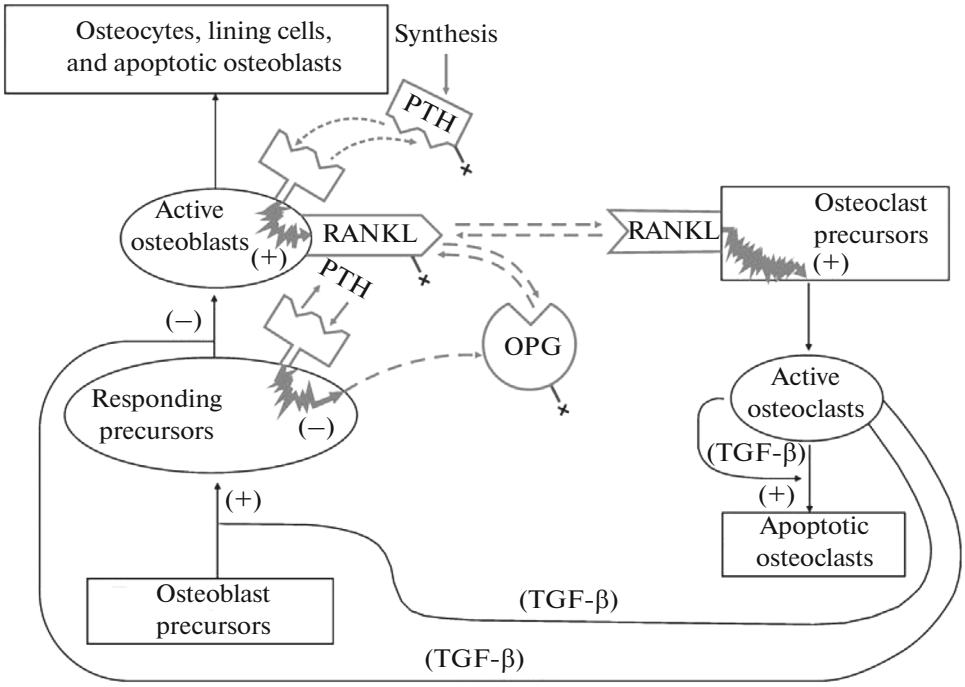

Fig. 1. The scheme of the processes considered in the model describing the interactions of active osteoblasts and osteoclasts [13]: ovals, cell types considered in the model and rectangles, cell types omitted in the model. Zigzag arrows denote the signaling pathways that lead to an increase (decrease) in the production of the corresponding agent (adapted from [13]).

ers, and active parathyroid gland cells) in compartment *y* (intercellular compartment, bone tissue, total pool of the body's cells, intestine, kidneys, and parathyroid glands) as the result of the total flow of component *x* into compartment *y*. The model accurately describes the published clinical data on the effect of calcium concentration in the plasma on the PTH secretion as well as the correlations of calcium concentration in plasma and urine of the patients with hypo- and hyperfunctions of the parathyroid glands. The model has demonstrated its utility for analysis of the general mechanisms of the diseases associated with impaired calcium metabolism and their detailed characterization.

The bone tissue is constantly reconstructed. Osteoblasts (the cells that produce new bone tissue) and osteoclasts (the cells dissolving old bone tissue) concertedly function in a 3D mineral structure of the bone. The interaction between osteoblasts and osteoclasts provides the balance of growth and loss in the bone mass, which are processes that are tightly correlated. A chronic disturbance of biochemical or cellular associations between the bone cells results in metabolic diseases of the bone tissue. The model that takes the major mechanism of interaction between osteoblasts and osteoclasts was proposed by Lemaire et al. into account [13]. This model implements the idea that, on the one hand, the ratio of the pools of immature and mature osteoblasts controls the degree of activity of osteoclasts and, on the other hand, osteoclasts are able to release the cytokine that regulates osteoblast differentiation, and correspondingly, their activity, from the bone matrix into the local microenvironment (Fig. 1).

The model takes the fact into account that differentiation of osteoclast precursors and subsequent formation of active multinuclear osteoclasts results from the contacts of osteoclast precursors and active osteoblasts. Receptor activator of nuclear factor NF-κB (RANK), which is expressed on the surface of osteoclast precursors, and RANK ligand (RANKL), expressed on the surface of osteoblasts, are the agents for such contact. Note also that the osteoblast precursors secrete soluble osteoprotegerin (OPG) receptor into the intercellular space; this receptor interacts with RANKL and inhibits the RANK/RANKL interaction, thereby inhibiting activation of osteoclasts. The model takes the fact into account that active osteoclasts influence the pool of active osteoblasts by releasing transforming growth factor TGF-β from the bone matrix; TGF-β stimulates selection, migration, and proliferation of osteoblast precursors and concurrently inhibits the final stage of osteoblast differentiation. The model also takes the fact into account that PTH (together with vitamin D) is the most important hormone that regulates the reconstruction of bone tissue. At a steady state concentration in the plasma and when therapeutically administrated, PTH binds to the

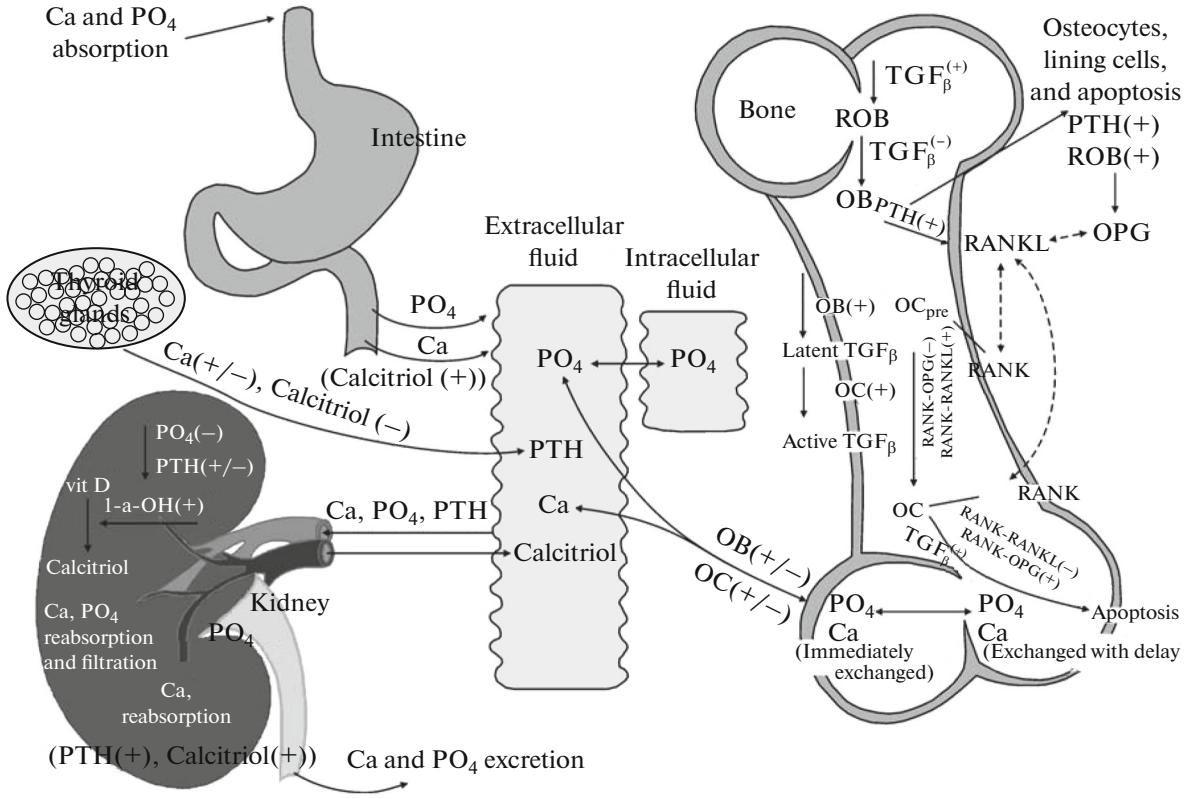

Fig. 2. The scheme of the processes considered in the integrated model of cell reconstruction and systemic homeostasis: OB, osteoblasts; ROB, pre-osteoblasts that differentiate into OB; and OC, osteoclasts (adapted from [16]).

PTH receptors of osteoblasts and stimulates PANKL production by inhibiting OPG production. This leads to an increase in the number of active osteoclasts. Thus, the RANK/RANKL/OPG pathway, as well as different effects of TGF-β on the osteoblast precursors at different stages of differentiation, play a key role in regulation of the bone reconstruction and form the basis of the model. The model consists of three differential equations that describe the dynamics of the pre-osteoblast, active osteoblast, and osteoclast pools.

This model has been used to compute the concentration dynamics for bone cells when the system is perturbed by addition or removal of one of the cell types (active osteoblasts, immature osteoblasts, or active osteoclasts) at a constant rate as well as by a long-term exposure (60 days) of the system to PTH, RANKL, or OPG. The model allows the specific features in reconstruction of the bone tissue to be clarified. In particular, an increase in the concentration of osteoclasts is observed during continuous addition of PTH or RANKL to the system versus addition of OPG, which causes a rapid decrease in the concentration of osteoclasts on the background of a considerably slower decrease in the concentration of osteoblasts. The model has also demonstrated that the balance between bone formation and destruction is determined by the RANKL/OPG ratio, which eventually determines the osteoclast to osteoblast (C/B) ratio in the system as an important therapeutic characteristic (for example, when administering PTH or glucocorticoids). The parameters for the model were assessed based on the published data. One of the interesting model results is that the calculated C/B ratio is 1.25 for the bone with a constant mass (homeostasis). The relevant literature gives this ratio in the range of 0.28–1.47 [14, 15]. That simulate the conditions of bone diseases (deficiency in estrogen, vitamin D_3, TRG-β, or some others) are varied, the model demonstrates a good fit of the computed values for the changes in C/B ratio, total number of these cells (a characteristic of the bone tissue metabolism), and concentrations of bone cells to the clinical data. Variation of the corresponding parameters also allowed the authors to conclude that the therapy aimed at bone tissue formation is more efficient as compared with the inhibition of bone resorption.

Using the models described in [12, 13], Peterson and Riggs [16] constructed an integrated physiologically justified model of calcium homeostasis and bone reconstruction; the model includes description of the intracellular anti-apoptotic Runx2–Bcl-2–CREB signaling pathway in osteoblasts induced by intermittent PTH administration [17]. The scheme of the pro-

cesses considered in the model is shown in Fig. 2. The goal of the work was to construct a model that would make it possible to study the causes and state of diseases, as well as therapeutic effects in patients.

Unlike models [12] and [13], the integrated model [16] allows for study of the bone remodeling taking the regulation and maintenance of the systemic homeostasis in the human body into account. The initial minimal models were extended when constructing the integrated model. In particular, the integrated model considers in more detail the exchange of calcium and phosphates between the bone and plasma, activity regulation of bone cells with involvement of TGF-β and PTH, and apoptosis in osteoblasts with involvement of Runx2–Bcl-2–CREB control mechanism under intermittent administration of PTH. In addition, this integrated model describes the dynamics of RANK, RANKL, and OPG, which are the key players in the interaction of osteoblasts and osteoclasts. Involvement of these molecules has made it possible to simulate formation of the RANK/RANKL and RANKL/OPG complexes taking the effects of active TGF-β and PTH on these processes into account. The integrated model consists of 28 differential equations with 49 parameters and 19 hyperbolic functions describing the effect of a variable on the dynamic of other variables. Five parameters that characterize the degradation rate constant for PTH in the plasma, exchange of phosphate between the plasma and bone tissue and between the plasma and cells of the overall body, and calcitriol production and elimination were taken from the model described in [12]. The remaining parameters of the model equations were estimated by fitting the model solutions to various clinical data, including the data obtained before, during, and after the therapy aimed at a growth in bone tissue density or inhibition of its resorption and the data for the patients with parathyroid disturbances and different degrees of kidney failure. The model accurately describes the published data on the long-term concentration dynamics of PTH, Ca^{2+}, and biochemical markers of osteoblast and osteoclast functions in the patient's plasma during denosumab (monoclonal antibodies to RANKL) therapy [18]. The model also accurately describes the long-term concentration dynamics of the osteoblast and osteoclast function markers in the plasma during teriparatide (PTH 1-34) therapy [19]. Moreover, the model allows for prediction of the concentration dynamics of other important plasma characteristics (phosphate, calcitriol, and others) during denosumab and teriparatide therapies that fit the clinical data [20]. The model predicted a severalfold increase in the concentrations of PTH and biochemical markers of osteoclast function by the end of a 12-month period in patients suffering from primary hyperthyroidism (a progressive growth in endogenous PTH concentration in the plasma) compared with the norm, as well as a considerable increase in the concentrations of Ca^{2+} and biochemical markers of osteoclast function and an elevated phosphate concentration in the plasma. The value and direction of each predicted effect matched the corresponding clinical data [21]. In the case of secondary hyperthyroidism caused by progressive renal failure, the model demonstrated entirely different concentration dynamics for the PTH, calcitriol, phosphate, Ca^{2+}, and the biochemical markers of osteoblast and osteoclast functions in the plasma. Model calculations matched the relevant clinical data [22]. For primary hypothyroidism (a decrease in the endogenous PTH in the plasma to 50%), the model predicted a considerable decrease in the concentrations of Ca^{2+}, as well as biochemical markers of osteoblast and osteoclast function, a certain decrease in the calcitriol concentration, and an almost constant concentration of phosphates in the plasma, which agrees with the clinical data [23]. Thus, the integrated model quantitatively describes the cellular aspects and key control mechanisms that underlie bone reconstruction and calcium homeostasis and significantly contributed to the insight into intricate dynamic processes of the physiology of bone tissue and the endocrine system, as well as the relevant clinical and therapeutic effects.

INTEGRATED MODELS FOR THE HEPATITIS C VIRUS–HOST SYSTEM

Hepatitis C virus (HCV) infection has become a global problem, since over 180 million people are already infected with this virus [24]. HCV infection progresses into a chronic frequently asymptomatic disease of the liver eventually leading to cirrhosis and liver cancer [25]. Mathematical models have been developed to study the mechanisms that underlie the interactions between the virus and host as well as HCV dynamics during its treatment. The models of cell infection by HCV that describe the infection in the body and effects of the therapy while omitting intracellular processes have been most actively developed [26–32]. Recently, deterministic models that comprehensively describe the intracellular processes of HCB RNA replication and the effects of therapeutics on these processes have been also constructed [35]. A stochastic model was recently proposed to describe intracellular RNA replication of wild-type HCV in fine detail, as well as the emergence and production of drug-resistant mutants and the effects of new anti-HCV therapeutics on these processes [6].

The first model that describes HCV infection in interferon-α (IFN-α) therapy at the level of the overall body was proposed by Neumann et al. [26]. This model consists of three differential equations that describe the dynamics of target cells (T), infected cells (I), and virus (V) with the rate constants for target cell production (s) and death (d), infection by the virus

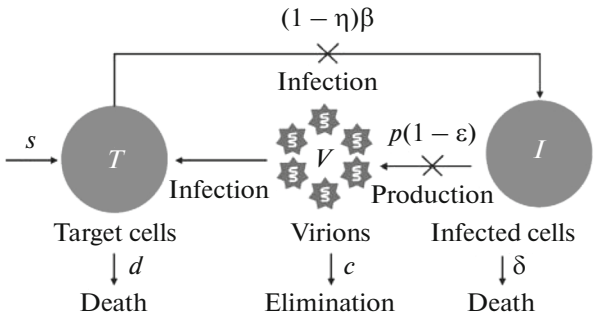

Fig. 3. The scheme of the processes considered in the standard kinetic model [26]. Target cells (*T*) are produced with a rate constant *s*, die with a rate constant *d*, and are transformed into infected cells (*I*) by virus (*V*) with a rate constant β. Infected hepatocytes die with a rate constant δ. Virus *V* is produced by cells *I* with a rate constant *p* and are eliminated from the system with a rate constant *c*. It is assumed that IFN-α therapy blocks the new infection with an efficiency ε (adapted from [26]).

circulating in the HCV–host system (β), death of infected cells (δ), production of free virions (*p*), and elimination of virions from circulation (*c*). It was assumed that IFN-α blocks new infection of cells *T* and production of virions by cells *I* with efficiencies η and ε, respectively (Fig. 3).

The model parameters were estimated using the clinical data on a decrease in HCV RNA in the patient's blood by IFN-α therapy, as well as the relevant literature data. The model accurately describes a two-phase dynamics of a decrease in HCV RNA in the plasma during IFN-α therapy. These dynamics comprise the initial phase with a rapid decrease in HCV RNA during the first 1–2 days of the therapy and the second slower phase of this decrease. The model demonstrates that the efficiency of HCV RNA decrease in the first phase is determined by the rate of virus elimination from circulation, *c*, versus the second phase, when the key parameter is the mortality rate of infected cells, δ, which considerably varies for individual subjects (being even zero in some cases). The model has been considerably modified in order to make it more realistic and able to explain other types of HCV RNA dynamics during IFN-α therapy and new therapies utilizing the drugs that act on the viral targets in infected cells [27, 28]. The proliferation of infected and uninfected hepatocytes are taken into account in this model [27, 28] by adding a new parameter *r*, related to the maximum rate of hepatocyte proliferation; this made it possible to explain a three-phase kinetics of the decrease in viral RNA during IFN-α therapy and its frequently observed increase after the therapy is completed, including restoration to an initial level. Note that adaptation of this model [27, 28] gave realistic values for the mortality rate constant of infected cells, δ. Another modification adapted the model to study the development of HCV drug resistance to telaprevir, a specific inhibitor of HCV NS3 protease; drug-sensitive wild type (*Vs*) and drug-resistant mutant (*Vr*) virus variants are additionally considered [29]. It is assumed that *Vs* and *Vr* infected cells *T* to give two types of infected cells (*Is* and *Ir*). The model was supplemented with new parameters related to the rate of *Vs* and *Vr* virion production (p_s and p_r), inhibition efficiency of *Vs* and *Vr* virions for telaprevir (ε_s and ε_r), and the probability that cells *Is* produce drug-resistant virus *Vr* (μ). The values of the parameters were assessed utilizing published and clinical data. The model succeeds in explaining a complex dynamics of HCV RNA with the initial (rapid) and second (slow) phases of decrease in HCV RNA and the third phase of an increase in HCV RNA in the case of telaprevir monotherapy. The model accurately describes the dynamics of HCV RNA for the combined therapy with telaprevir and IFN-α on the assumption that the virus variant resistant to telaprevir, *Vr*, is sensitive to IFN-α.

Other models [30, 36] constructed based on the model described in [26] take the pharmacokinetics of NS3 protease inhibitors (telaprevir and boceprevir) into account by adding the parameter ε as a function changing with time. This makes it possible to describe the long-term dynamics of HCV RNA of the patients treated with these inhibitors and explain the higher efficiency of this therapy compared with the IFN-α variant.

The model described in [26] was used to construct a multi-variant viral dynamic model [31] to assess the replicative ability in vivo of HCV drug-resistant mutants (A156V/T, V36A/M, R155K, T54A, and V36M/R155K) that are frequently present in the patient's plasma during telaprevir therapy and to compute the HCV RNA dynamics for these variants, wild type, and total HCV RNA dynamics. This model takes the infection of cells *T* by virus *Vi* giving variant-*i*–infected cells, *Ii*, into account based on the assumptions that each cell *Ii* is infected by one variant, cells *T* represent a limited replication space for all variants, and each cell *Ii* produces the populations of both virus *i* variant and mutant virus *j* fraction. The model is constructed on the assumption that the parameters of mutation rate (*m*), production of target cells (*s*), virus death (*c*), infection rate (β) and target cell death (*d*) are the same for different variants of virus *Vi*, while the production parameters (pf_i) and the efficiency of suppression of virion production (ε_i) depend on the type of mutant. It was also assumed that the mortality rate of infected cells (δ_i) is constant for different virus variants in IFN-α therapy and depends on the type of mutant in telaprevir therapy. This approach [32] additionally considers pharmacokinetics of telaprevir and IFN-α/ribavirin, which has allowed for prediction of RNA dynamics for the wild-type and mutant viruses as well as total HCV RNA based on a large cohort of

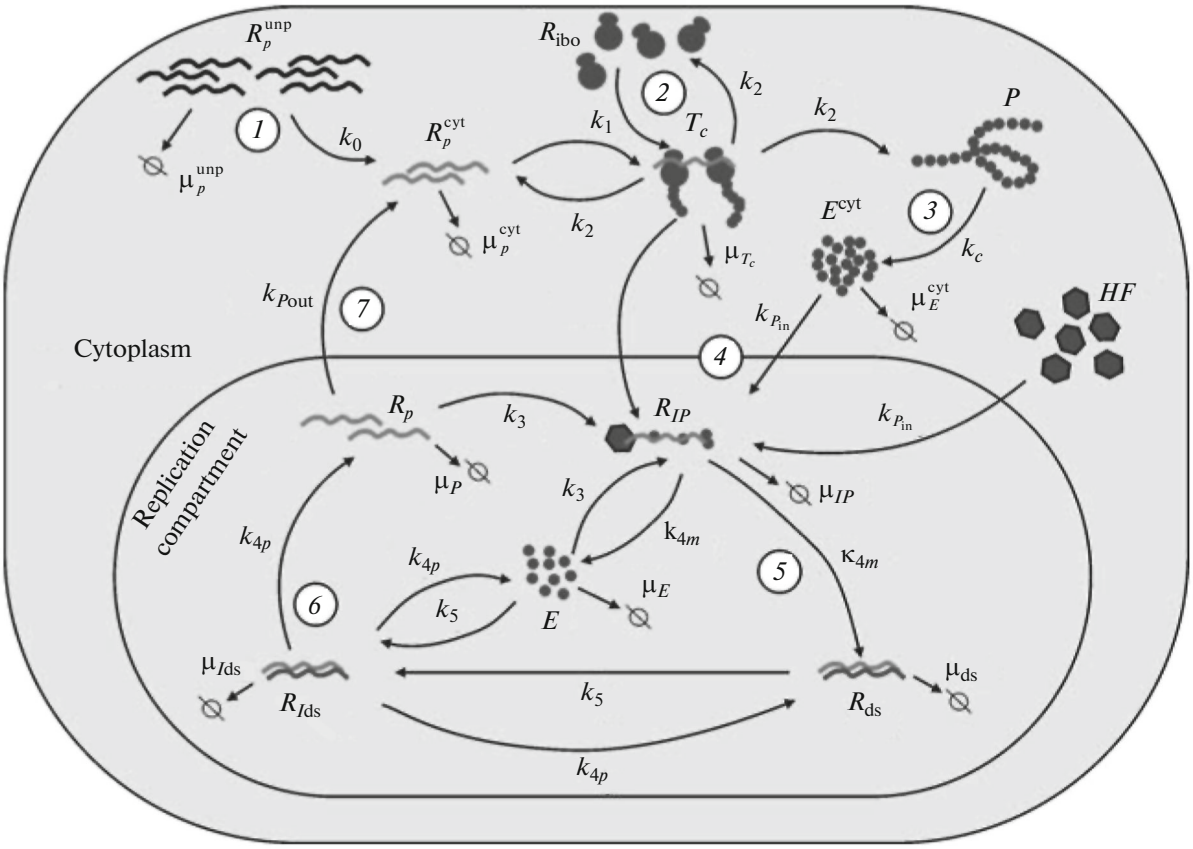

Fig. 4. The scheme of the intracellular processes of HCV RNA replication in the model described in [34]: (*1*) HCV plus-strand RNA, R_p^{unp}, enters the cell cytoplasm by transfection and is structurally remodeled to give translation-competent RNA, R_p^{cyt} (rate constant, K_0); (*2*) ribosomes R_{ibo} bind R_p^{cyt} into translation complex T_c (rate constant, k_1); the complex translates RNA into polyprotein P (rate constant, k_2); (*3*) polyprotein P is processed to give mature viral proteins E^{cyt} (rate constant, k_c); intracellular membrane vesicles, viral replication compartments in the cell, are formed in the presence of viral proteins; (*4*) viral proteins E^{cyt}, associating with one another to give replicase, one or several host factors *HF*, and actively translated RNA plus strand of the translation complex T_c are imported to membrane vesicles to form replication initiation complex, R_{IP}, for RNA plus strand (rate constant, k_{Pin}); (*5*) replication complex R_{IP} produces complementary RNA minus strand within double-stranded RNA, R_{ds} (rate constant, k_{4m}); (*6*) in turn, RNA minus strand within R_{ds} after forming the corresponding initiation complex R_{Ids} (rate constant, k_5) with involvement of viral proteins E serves as a template for synthesis of the RNA plus strand (rate constant, k_{4p}); (*7*) RNA plus strand R_p is exported from the membrane vesicles to cytoplasm (rate constant, R_{Pout}), where it can again be translated into polyprotein P or remain in the vesicles to give new replication initiation complexes for RNA plus strand R_{IP} (rate constant, k_3); adapted from [34].

patients subject to a combined therapy with telaprevir and IFN-α/ribavirin.

A deterministic model of intracellular replication of the HCV subgenomic replicon was proposed by Dahari et al. [33] for the first time. This model describes the main intracellular processes that underlie the replication of subgenomic replicon, including the viral RNA synthesis in membrane vesicles. The model implies that the number of ribosomes involved in translation of the viral genome is limited. This makes it possible to control the unlimited growth of viral RNA and proteins in the cells. In general, the model accurately describes the production of viral RNA and proteins, as well as their arrival to steady state concentrations after the cells are transfected with HCV RNA replicon but it fails to reproduce the experimentally observed decrease in the viral components in the presence of drugs. Concurrently, another model of intracellular replication of the HCV subgenomic replicon that explicitly contained the mechanisms that underlie the effects of drugs on the viral and cellular targets was proposed [35]. Unlike the model by Dahari et al. [33], this model contains the cellular factor involved in formation of replicative complexes, which controls the unlimited increase in the amounts of viral

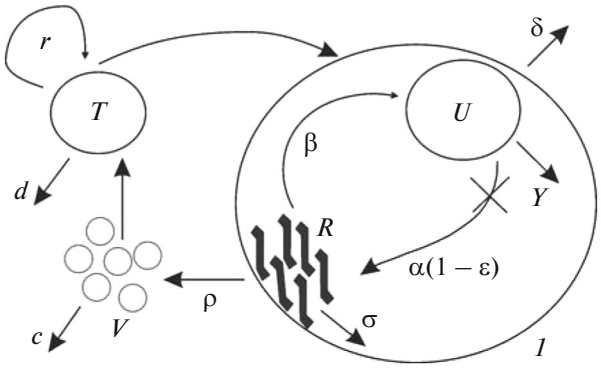

Fig. 5. The scheme of the model by Guedj and Neumann [44], which takes HCV intracellular replication and cell infection into account. The virus RNA, *R*, is translated and transcribed in infected cell *I* to give replicating units *U* (rate constant, β). In turn, replicating units *U* synthesize HCV RNA *R* (rate constant, α) and die (rate constant, γ); ε is the blocking efficiency of *R* synthesis by the inhibitors of HCV RNA polymerase NS5B. RNA *R* is also involved in formation of virus *V* and its secretion from cell *c* (rate ρ*R*(*t*) per cell). Virus *V* is able to infect cells *T* (rate constant, *b*); adapted from [44].

RNA and proteins. This allowed this model [35] to accurately describe the effect of drugs on the dynamics of intracellular steady state concentration of HCV RNA for short-term (to 3 days) exposure to drugs. A model proposed later [34] for the replication of subgenomic HCV RNA replicon was based on the model described in [33]; this model also contains a cellular factor analogous to that in [35]. The scheme of the HCV RNA replication processes that were taken into account in [34] is shown in Fig. 4.

The above-mentioned model [34] has made it possible to describe the specific features for how the viral RNA reaches a steady state after transfection in the cell lines that differ in the initial concentrations of cellular factor *HF*. However, this model omitted the mechanisms of drug action, similarly to [33].

Numerous recent papers have described administration of anti-HCV drugs that directly attack the HCV NS3 protease and NS5B polymerase, as well as the HCV NS5A protein, involved in the virus replication [37, 38]. These drugs decrease the HCV RNA in both the first and second phases of its dynamics considerably faster compared with IFN-α administration [39–43]. The need to study the effects of these drugs with the use of mathematical models stimulated construction of models containing descriptions of specific intracellular interactions between the drugs and viral targets. Correspondingly, the multi-scale models consider the virus–host interactions in the presence of drugs both at the levels of cells and intracellular level. The first model that described the HCV dynamics was the model by Guedj and Neumann [44]. This model can be regarded as an extension of [26] obtained by addition of two new variables that describe intracellular processes of viral RNA replication: $R(t)$ is the number of genomic HCV RNA plus strands that are available for transcription and translation and $U(t)$ is the number of replication units (the number of minus strands within the double-stranded HCV RNA) that are available for synthesis of the genomic plus strands. It was assumed that R is the template for formation of replication units U, which, in turn, are the template for synthesis of R. The limitation for production of units U is specified by parameter U_{max}. The intracellular replication dynamics and dynamics of cell infection are linked by replacing the rate of virus production by infected cells, $p = \text{const}$ [26], with the function $p(t) = \rho R(t)$. The intracellular antiviral effect of the drug is simulated by introducing the parameter ε that reflects the blocking efficiency for the synthesis of HCV RNA plus strands (Fig. 5). The HCV resistance to the drug is taken into account by introducing several variables to the model, such as R^{wt} and R^{res} (RNA plus strands of the wild-type and drug resistant variants); U^{wt} and U^{res} (replicating units of the wild-type and drug-resistant variants within each infected cell); and V^{wt} and V^{res} (wild-type and drug-resistant virus types, respectively).

To describe the processes of viral RNA replication, eight parameters were added to the model by Guedj and Neumann [44], including the rate constants for formation and degradation of replication units (β and γ), RNA export from infected cells (ρ), and synthesis of wild-type and mutant HCV RNA (α^{wt} and α^{res}). The model showed a fast continuous decrease in HCV RNA in the absence of virus drug resistance, i.e., the dominance of its wild type during the therapy and a high antiviral effect of the drug; the slope of the second phase is proportional to the intracellular parameter γ (mortality rate of replicating units). The patterns of HCV RNA dynamics under selection of drug-resistant HCV variants during the therapy depend on the degree of drug resistance and replicative ability of these variants. A high degree of drug resistance and a high replicative ability of HCV variants lead to the dynamics with the initial rapid decrease in its RNA followed by its growth to a new steady state, lower compared with the level before the therapy. The average degree of drug resistance and average replicative ability of HCV variants result in the dynamics with the initial rapid decrease in RNA followed by its temporary growth and eventual continuous decrease; the efficiency of this decrease is determined by the δ parameter (the rate of infected cell death).

Another multi-scale model constructed for computation of drug effects that directly influence the viral targets involved in the viral RNA intracellular replication was proposed by Guedj et al. [45]. This model extends the standard model [26] by adding the variable

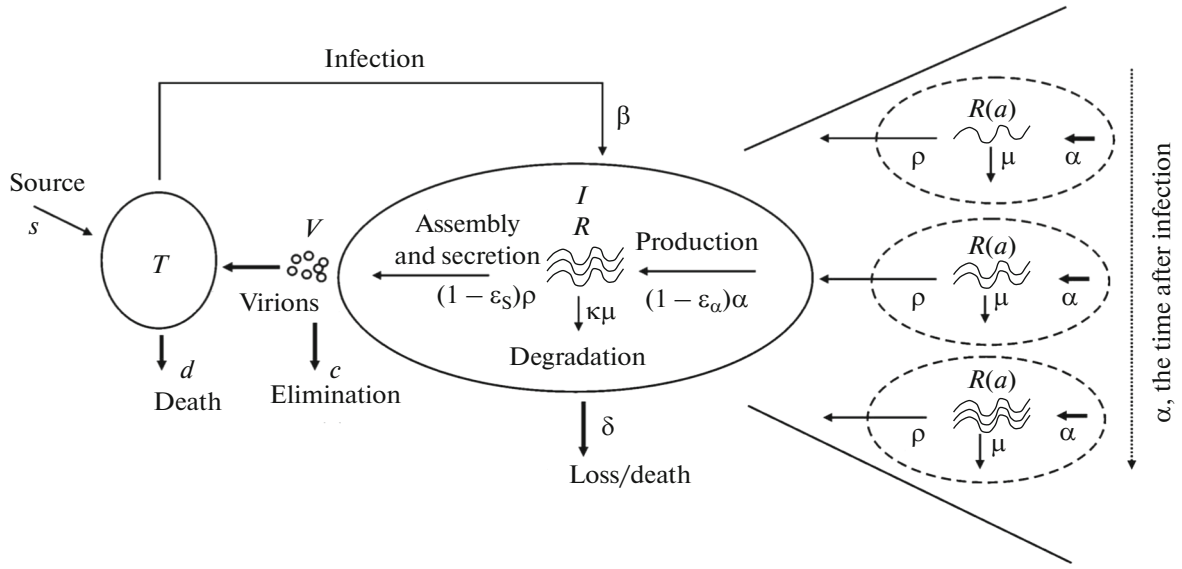

Fig. 6. The scheme of the multi-scale model by Guedj et al. [45]: *T*, target cells, which are produced and killed (rate constants, *s* and *d*, respectively); *I*, infected cells, dying with the rate constant δ; *V*, virus infecting cells *T* (rate constant, β) and killed (rate constant, *c*); *a*, age of infection (the time span from the moment the first virion carrying RNA genome enters cell *T*); *R*(*a*), intracellular viral RNA, which is produced in the cell at the rate α, degraded (rate constant, μ), and is involved in virus assembly/secretion (rate constant, ρ). The efficiency of drug in blocking RNA production, virus assembly/secretion, and increase in RNA degradation in the cell are ε_α, ε_s, and *k*, respectively (adapted from 45].

R(*t*), intracellular HCV genomic RNA. The authors assume that *R* is produced in the cell at a constant rate α, is degraded with the rate constant μ, and is involved in virion assembly/secretion with the rate constant ρ. The authors assume that α depends on the age of the infection, i.e., on the time period from the moment the first virion carrying the RNA genome enters the cell. The scenario is considered where the therapy with drugs that attack the viral targets involved in HCV RNA replication commences when the HCV RNA attains the intracellular steady-state concentration and blocks viral RNA production, assembly/secretion of the virus, and increases HCV RNA degradation with efficiencies ε_α, ε_s, and κ, respectively. Unlike the standard model [26], which does not describe intracellular processes associated with HCV RNA, this model makes it possible to distinguish different potential intracellular effects of therapy. This model was constructed to comprehensively examine the kinetics of decrease in HCV RNA at the initial period of drug administration (to 2 days) and, therefore, does not consider the emergence of drug-resistant HCV variants and their production in infected cells (Fig. 6). Compared with the standard model [26] (Fig. 3), the integrated model [45] additionally includes α, μ, ρ, ε_α, ε_s, and κ parameters. The estimate for the parameter δ fits the corresponding value averaged over different patients examined in [26]. The remaining parameters were estimated using the kinetics of changes in HCV RNA during the therapy with daklatasvir, an inhibitor of the HCV NS5A protein.

The model was constructed to explain rapid kinetics of a decrease in HCV RNA in the patients treated with a single daklatasvir (BMS-790052) dose (the level of HCV RNA in the serum decreased by approximately two orders of magnitude over the first 6 h after drug administration). The kinetics of decrease in HCV RNA during the therapy with a single daklatasvir (BMS-790052) dose have three phases; the first phase, 6–7 h after drug administration; the second, from 6–7 h to 2 days; and the third, over 2 days after drug administration. The model has shown that these phases are determined by parameters *c*, *k*μ + δ, and δ, respectively. It has emerged that BMS-790052 has two main modes of action on the virus: (1) efficient blocking of intracellular synthesis of viral RNA and assembly/secretion of virions and (2) increase in the rate of intracellular degradation of HCV RNA. The model demonstrated that the first phase in the kinetics of viral RNA decrease can be experimentally observed only in the case of very efficient blocking of virion assembly/secretion ($\varepsilon_s \sim 1$), which is the case of daklatasvir. Correspondingly, this phase in the kinetic pattern of the change in RNA is unobservable for IFN-α therapy; instead, the second phase is observed first. The model estimate for the average half-life of HCV particles in the serum is ~45 min. This corresponds to $c = 22.3$ days^{-1}, which is approximately four times higher compared with the average estimate for parameter *c* in the standard model [26]. The integrated model also accurately describes the kinetics of a decrease in HCV RNA for the therapy with telaprevir,

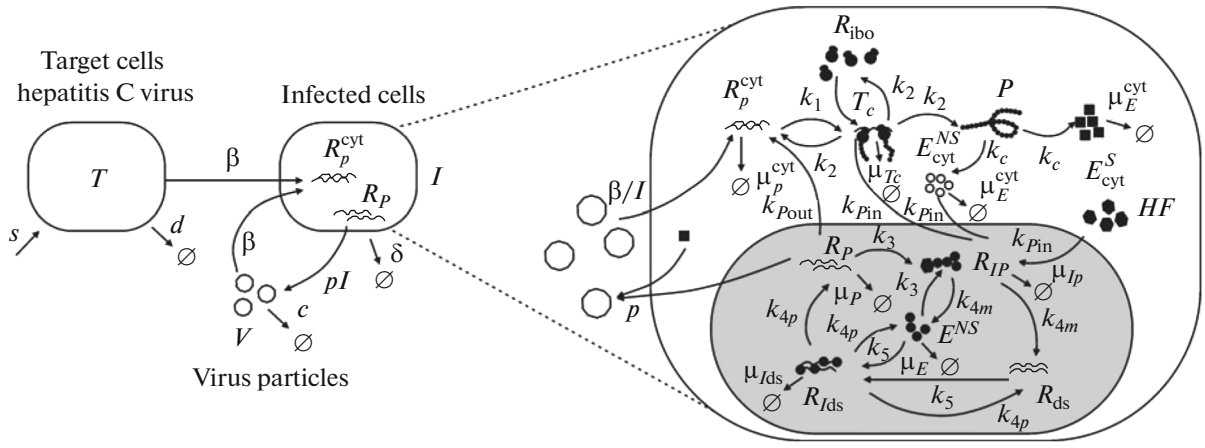

Fig. 7. The scheme of the processes considered in the integrated model by Clausznitzer et al. [47]. Target cells T are produced (rate, s), killed (rate, d), and transformed into cells I infected by virus V. Virus V enters the cell as an RNA plus strand, R_p^{cyt}. In the cytoplasm, R_p^{cyt} binds to cell ribosomes R^{ibo} to form translation complex Tc, which translates R_p^{cyt} into polyprotein P. This polyprotein is processed (cleaved) to give viral polymerase, E_{cyt}^{NS}, and structural proteins, E_{cyt}^{S}. The RNA from the translation complex T_c together with E^{NS} polymerase and host factor HF form the corresponding replication initiation complex R_{IP} in the membrane replicative compartment of the cell (membrane vesicles), which, in turn, produces double-stranded RNA intermediate, R_{ds}. After the interaction of E_{cyt}^{NS} polymerase with R_{ds} intermediate, the corresponding replication initiation complex R_{Ids} is formed. This complex produces a new RNA plus strand, R_p. The synthesized R_p can again enter the replication cycle and associate with viral structural proteins E_{cyt}^{S} with assembly/export of viral particles V (adapted from [47]).

an NS3 protease inhibitor, and demonstrates that daklatasvir efficiency in blocking the assembly/secretion of viral particles is 30 times higher compared with telaprevir. Rong et al. [46] performed a comprehensive mathematical analysis of the integrated model [45], as well as examining the kinetics of a decrease in HCV RNA in the therapy with danoprevir, an NS3 protease inhibitor. This analysis shows that the main modes in the danoprevir effect are blocking of the intracellular HCV RNA production, an increase in intracellular RNA degradation, and a moderate inhibition of the assembly/secretion of HCV particles.

Unlike the above-described multi-scale models [44–46], which consider only the main intracellular processes of HCV RNA replication and assembly/secretion of viral particles, the multi-scale model by Clausznitzer et al. [47] represents the intracellular processes of HCV RNA replication in detail. This model [47] is based on integration of the models of cell infection by HCV [26] and replication of HCV RNA subgenomic replicon in cells [34]. This integration into a multi-scale model made it necessary to add a new variable to the model describing the number of structural proteins in the cell (E_{cyt}^{S}) and a description of the formation/export of the viral particles via the interaction of E_{cyt}^{S} and RNA plus strand (R_p). The addition of these processes to the integrated model required new rate constants, namely, for the formation/export of viral particles (p), blocking of RNA plus and minus strands (e_s), and virus assembly/secretion (e_p) during daklatasvir (an inhibitor of HCV NS5A) therapy. The scheme of the processes described by the model is shown in Fig. 7.

The integrated model [47] contains 13 ordinary differential equations. All parameters for the description of intracellular processes except for the interactions with host factor, *HF*, were taken from the model by Binder et al. [34]. *HF* concentrations and parameters e_s, e_p, and p were estimated for each patient based on the kinetic data for the changes in viral RNA during daklatasvir therapy. The model accurately describes the dynamics of a decrease in viral RNA during 2 days after administration of a single dose of daklatasvir, an inhibitor of HCV NS5A protein. According to the literature data, the viral protein NS5A is involved in both the synthesis of viral RNA [48] and assembly of the viral particle [49, 50]. This integrated model [47] makes it possible to examine the effects of the drugs that directly influence the specific intracellular molecular processes that underlie HCV replication that are observed during 2–3 days. The model is useful for optimizing therapeutic schemes and predicting the effects of combined therapy, for example, daklatasvir with inhibitors of HCV NS5B polymerase or IFN-α.

The above-described methods for integrating models require the knowledge about all players that determine the interactions between subsystems as well as numerical values for these interactions, which considerably complicates application of these approaches. A new approach to integration of the models that describe dynamics of two and more molecular genetic networks when the available data on their interactions are insufficient has been recently proposed [10]. The authors introduced the concept of mosaic gene networks for describing the complex systems of this type. The main idea of this approach is the use of a control functional, by means of which one subsystem of a mosaic gene network can control the function of another subnetwork. The authors considered the integration of two subsystems for a unilateral control when only one subsystem influences the dynamics of the other [10]. A linear function that depends on the concentrations of the variables of the control subsystem was used as the control functional. This function was in the right-hand part of the system of differential equations that described the controlled subsystem. The fact that the use of a linear control functional made it possible to achieve a good fit between the dynamics of the complete network and its mosaic analogs was rather unexpected. Mosaic networks were generated with the use of computer experiments by removal of certain fragments from the complete network to separate it into two unconnected subsystems.

This approach was applied to integrate the models for replication of the HCV subgenomic replicon [34] and the TNF-α–induced signaling pathways of apoptosis and activation of NF-κB transcription factor [51] in cells, which gave the description of how HCV is controlled by these signaling pathways. The parameters of the control functional were determined based on the experimental data from gene expression screening of one of the subnetworks in response to perturbations of the elements in the other subnetwork. The authors considered expression inhibition or activation of specific genes, including both host and pathogen genes as the perturbation of subnetwork elements. The integrated model [10] showed that HCV is most efficiently controlled via the *RIP*, *TRADD*, *TRAF2*, *FADD*, *IKK*, *IkBa*, *c-FLIP*, and *BAR* genes. The computed dynamics of the *RIP*, *TRADD*, *TRAF2*, *FADD*, *IKK*, *IkBa*, *c-FLIP*, and *BAR* genes in cells over 72 h after the cell culture was infected with HCV demonstrated a good fit to the experimentally observed expression dynamics of these genes [52]. In particular, analysis of the model shows that even a small increase in *c-FLIP* expression can significantly block induction of apoptosis. The predictions of the roles of the *TRADD*, *TRAF2*, *FADD*, *IKK*, *IkBa*, and *c-FLIP* genes in the regulation of apoptosis and NF-κB activation signaling pathways by HCV agreed well with the previously published data [53, 54].

INTEGRATED MODELS THAT DESCRIBE PHYSIOLOGICAL PROCESSES IN THE HUMAN BRAIN

State-of-the-art technologies for functional visualization, namely, functional magnetic resonance imaging (fMRI), magnetic resonance spectroscopy (MRS), positron emission tomography, and electromagnetic encephalography play an important role when studying the activation of human brain neurons in response to sensory, locomotive, or cognitive events. fMRI is used to record high-frequency signals that reflect one of the parameters that characterize regional neuronal brain activity, for example, a change in the regional cerebral blood flow or a change in the oxygen content in the blood. In particular, positron emission tomography records the γ-radiation that reflects the intensity of glucose uptake by neurons. Electromagnetic encephalography makes it possible to record very weak electric and magnetic fields and their gradients generated by the concerted activity of a neuron population. MRS is useful for recording the concentrations of various metabolites of neurons, such as *N*-acetylaspartate, choline, creatine, phosphocreatine, lactate, and ATP. However, a physiological interpretation of the results obtained by these methods is still a challenge.

An integrated mathematical model was constructed for interpretation of fMRI and MRS data [55]; this model describes the dynamics of synchronous processes in neurons in response to a stimulatory event, including hemodynamic, metabolic, and electrophysiological events. The authors integrated the model of glycolysis in erythrocytes [56, 57] and the model of oxygen transport across the blood–brain barrier [58] by introducing links between the electric activity of the postsynaptic membrane in neurons, neuronal energy metabolism, and hemodynamics. The scheme of the processes taken that were into account in the model is shown in Fig. 8. The model is based on the assumption that stimulation of the brain increases the membrane transport of Na^+ ions into neurons. The increase in intracellular Na^+ concentration activates the Na pump or Na/K-ATPase, which by reducing the initial membrane potential extrudes three Na^+ ions from the cell and accumulates two K^+ ions using the energy of one ATP molecule. In turn, the change in the intracellular ATP/ADP ratio stimulates ATP regeneration via three main processes: the buffer effect of phosphocreatine (reaction of phosphocreatine and ADP giving ATP and creatine), glycolysis (enzymatic reactions converting intracellular glucose into pyruvate and lactate yielding ATP), and mitochondrial oxidation of pyruvate by intracellular oxygen yielding ATP. The cells are supplied with energy substrates (glucose and oxygen) and freed from lactate via exchange with the cerebral blood flow across the blood–brain barrier. The cerebral blood flow

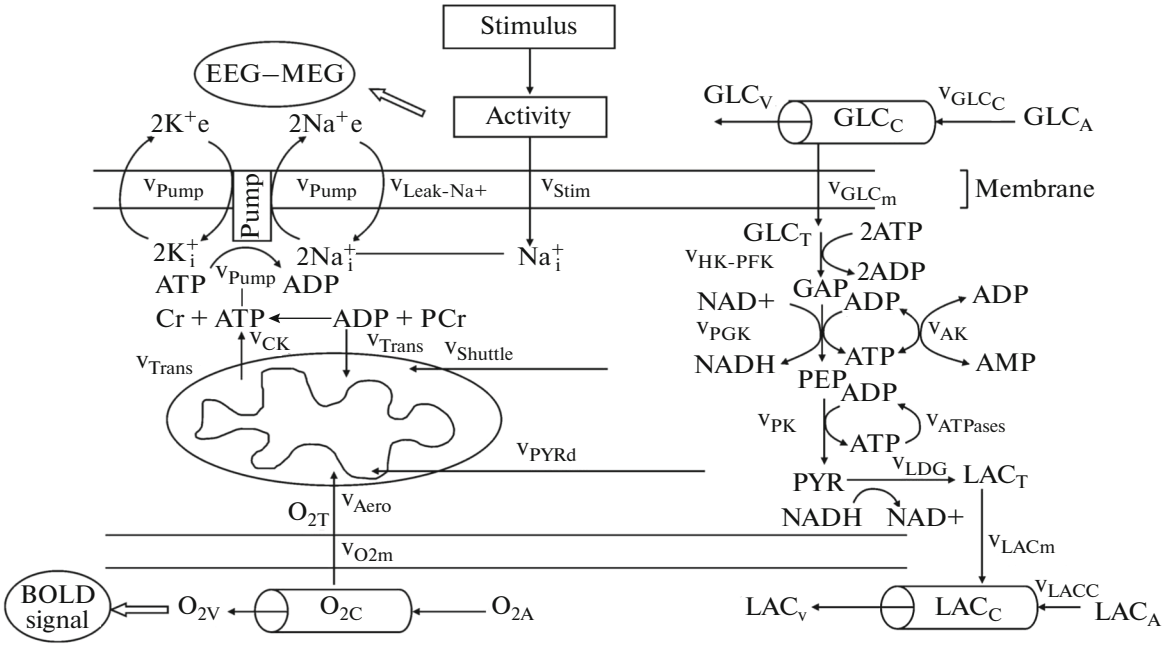

Fig. 8. The scheme of the processes involved in activation of neurons: GLC_T, intracellular glucose concentration; GLC_m, concentration of the glucose passing across the blood–brain barrier; GLC_A, arterial glucose concentration; GLC_V, venous glucose concentration; GLC_C, capillary glucose concentration; GAP, glyceraldehyde-3-phosphate concentration; HK, hexokinase; PEK, phosphofructokinase; PGK, phosphoglycerate kinase; AK, adenylate kinase; PEP, phosphoenolpyruvate; PK, pyruvate kinase; PYR, pyruvate concentration; LGH, lactate dehydrogenase; NADH, nicotinamide adenine dinucleotide (reduced form); NAD^+, nicotinamide adenine dinucleotide (oxidized form); LAC_T, intracellular lactate concentration; LAC_m, concentration of the lactate passing across the blood–brain barrier; LAC_A, arterial lactate concentration; LAC_V, venous lactate concentration; LAC_C, capillary lactate concentration; PUMP, Na/K ATPase; Cr, creatine concentration; PCr, creatine phosphate concentration; CK, creatine kinase; O_{2T}, intracellular oxygen concentration; O_{2m}, oxygen concentration in the blood–brain barrier; O_{2A}, oxygen concentration in arteries; O_{2V}, oxygen concentration in veins; and O_{2C}, oxygen concentration in capillaries (adapted from [55]).

increases with brain activation and influences the rate of glucose, oxygen, or lactate exchange across the blood–brain barrier.

The dynamics of many variables in the model by Aubert et al. [55] (glucose, lactate, ATP, phosphocreatine, and the level of cerebral blood deoxygenation) can be experimentally measured using MRS and fMRI. This model is useful for qualitative and quantitative testing of the hypothesis on physiological and biochemical processes involved in the activation of neurons, for example, on the character of mitochondrial activity during stimulation, change in the cerebral capillary flow during stimulation, concentration of intracellular oxygen, and the characteristics of the flexibility of veins. This allows a broad interpretation of the experimental data obtained by functional CT imaging.

Local changes in the content of deoxyhemoglobin per unit brain volume indicate its activation. The deoxyhemoglobin concentration is the main component of the blood oxygen level–dependent (BOLD) signal, which is measurable using fMRI. To theoretically calculate the dynamics of the BOLD signal [59], the model described in [55] was extended by incorporating the model by Buxton et al. [60]; according to this model the cerebral capillary volume during brain activation remains constant, while the venous volume V_v can change (dilatation). However, the change in V_v is delayed compared with the increase in the cerebral capillary blood flow $F_{in}(t)$ caused by stimulation. The dynamic of V_v is determined by the difference in the flows $F_{in}(t)$ and F_{out}, where F_{out} is the blood flow from venous dilatation, depending on V_v. The deoxyhemoglobin concentration in the brain tissue depends on $F_{in}(t)$, the level of cerebral oxygen metabolism, and V_v. The main physiological hypotheses of this integrated model [59] are shown in Fig. 9.

The authors demonstrated that the computed dynamics of the variables in this integrated model [59], including lactate, glucose, phosphocreatine, ATP, Na^+, BOLD signal, etc., fit the published MRS and fMRI data well for volunteers under a stable stimulation [61, 62]. The model has been also used to test the hypotheses on the mechanisms that underlie a decrease in the BOLD signal near brain tumors. According to experimental data, the cerebral blood flow is decreased in brain tumors and adjacent regions

[63]. The model shows that a decrease in the initial cerebral blood flow in quiescence, $F_{in}(0)$, leads to a decrease in the initial peak and steady-state level of the BOLD signal during stimulation, as well as an increase in the lactate peak under these conditions [64].

These models [55, 59] consider the interrelation between neurons and cerebral blood flow. It has been hypothesized [65] that part of the lactate secreted by astrocytes (glial cells of the brain) during brain stimulation can be taken up by neurons and act as an energy substrate for them, since the reaction of pyruvate conversion into lactate, as catalyzed by lactate dehydrogenase, is reversible (astrocyte–neuron lactate shuttle, ANLS). To test this hypothesis using the latter model [59], the authors constructed a model of the compartmentalized brain energy metabolism; this model consists of three compartments along with the blood vessels: astrocytes, neurons, and the intercellular space [65]. This model is based on the assumption that the brain stimulation in both cell types, that is, astrocytes and neurons, increases the Na^+ ion flux into the cells, while the subsequent activation of the Na pump activates ATP regeneration via the phosphocreatine buffer, glycolysis, and mitochondrial oxidation. The cells exchange oxygen, glucose, and lactate with the cerebral blood flow across the blood–brain barrier. Moreover, the model described the glucose and lactate exchange between the intracellular space, neurons, and astrocytes. The scheme of the processes described in the model is shown in Fig. 10.

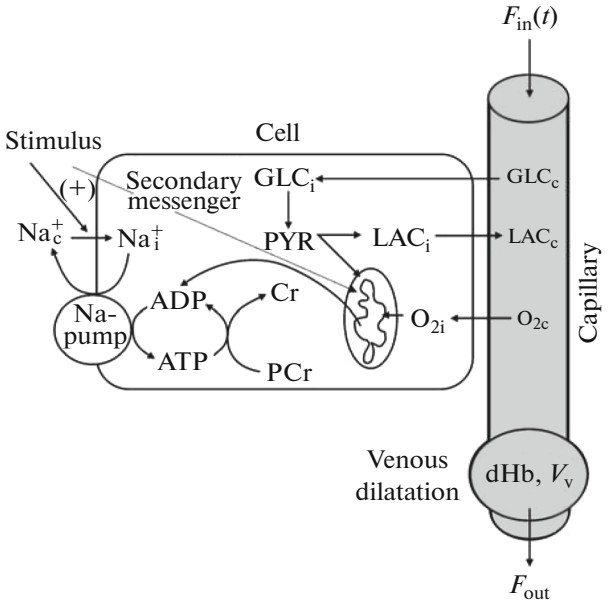

Fig. 9. The main physiological hypotheses of the model by Aubert and Costalat [59]: $F_{in}(t)$, regional cerebral blood flow through capillaries; F_{out}, the blood flow from venous dilatation; V_v, volume of venous dilatation; GLC_c, glucose concentration in capillaries; GLC_i, glucose concentration in cells; LAC_c, lactate concentration in capillaries; LAC_i, lactate concentration in cells; O_{2c}, oxygen concentration in capillaries; O_{2i}, oxygen concentration in cells; PYR, pyruvate concentration in cells; Cr, creatine concentration in cells; PCr, phosphocreatine concentration in cells; and PUMP, Na/K-ATPase (adapted from [59]).

In particular, the model described in [65] showed that ANLS occurs along with growth in neuronal glycolysis and depends on the relative stimulation intensity of neurons and astrocytes. In particular, ANLS at a low relative stimulation intensity of neurons continues over the entire period of stimulation and after its cessation; however, in the case of a high relative stimulation of neurons, ANLS occurs only at the beginning of stimulation and after it is stopped. The computed concentration dynamics of the extracellular lactate for both a single stimulation and periodically repeated stimulations fit the experimental dynamics of extracellular lactate in the rat brain hippocampus under analogous conditions well. This favors the idea that the lactate produced by brain astrocytes can be taken up by neurons and metabolized there to serve as an energy source [66].

The model described in [65] was used to construct a model of energy metabolism and hemodynamics in grade II (low malignancy) gliomas (primary brain tumors) [67–69]. It is known that low-grade gliomas undergo anaplastic transformation with an unfavorable prognosis; however, the period to such transformation varies for different subjects. Thus, insight into the evolution of gliomas is most important for timely therapy. An fMRI monitoring of the tumor volume allows observation of tumor development; however, the knowledge of metabolic and hemodynamic changes that underlie the pathophysiological mechanisms of gliomas transformation can provide earlier and more valuable data. The model described in [67–69] simulates the hemodynamics and lactate metabolism (lactate is an early marker of changes in the metabolism of tumor cells) in low-grade gliomas. The major variables of this model are the intracellular and intracapillary lactate concentrations, cerebral blood flow, lactate concentration in arteries, intracellular and intracapillary H^+ concentrations, intracellular and intracapillary volumes, and the maximum rate of lactate–H^+ transport across the blood–brain barrier (Fig. 11).

The values of the model parameters were determined by MRS and MRI of the blood flow and extracted from the relevant literature. This model is useful for examining the metabolism and hemodynamics in gliomas, as well as the search for new therapeutic strategies. As an example, analysis of the sensitivity of the model has predicted that changes in the model parameters, including a decrease in the regional cerebral blood flow and in the rate of the lactate transport across the blood–brain barrier, as well as an increase in the lactate concentration in arteries and

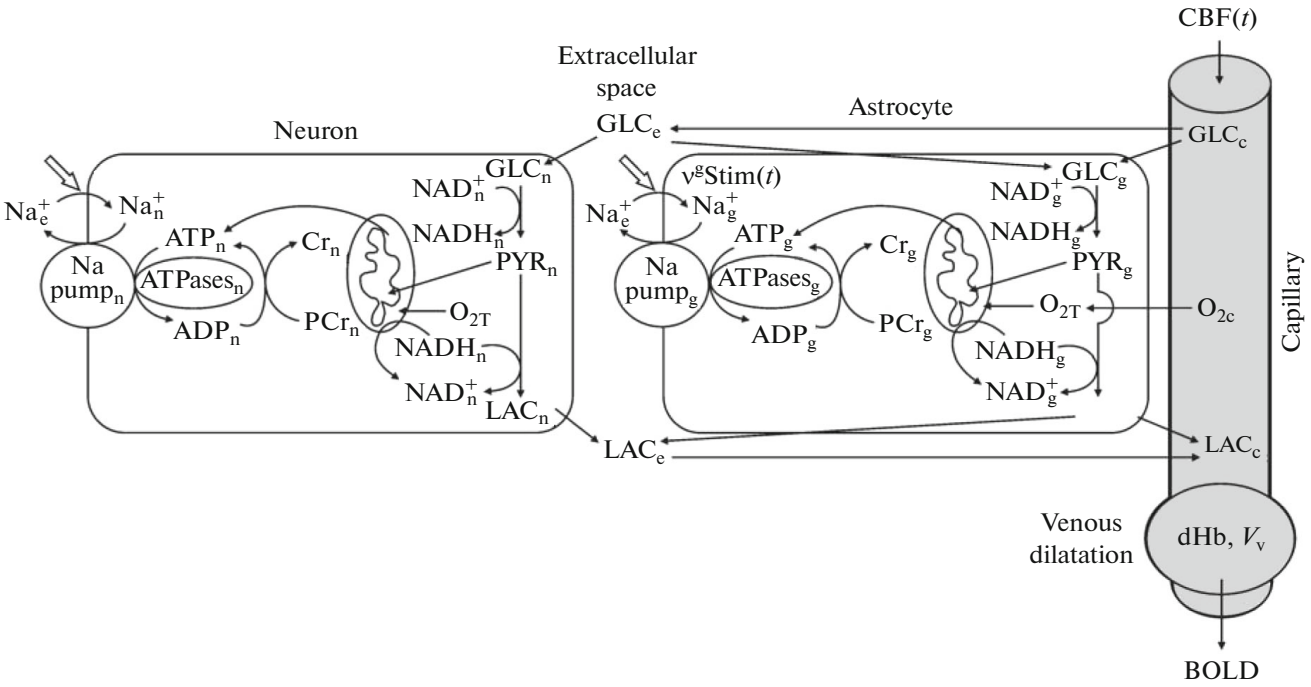

Fig. 10. The scheme of the processes described in the model of compartmentalized energy metabolism between astrocytes and neurons [65]. Each cell compartment contains all of the corresponding elements of the homogeneous model [59]. The intercellular space is the space for exchange between neurons and astrocytes. The regional cerebral blood flow through capillaries is designated CBF(t); dHb, deoxyhemoglobin; V_v, volume of venous dilatation; GLC_c, glucose concentration in capillaries; GLC_g, glucose concentration in astrocytes; GLC_n, glucose concentration in neurons; GLC_e, extracellular glucose concentration; PYR_g, pyruvate concentration in astrocytes; PYR_n, pyruvate concentration in neurons; LAC_c, lactate concentration in capillaries; LAC_e, extracellular lactate concentration; LAC_g, lactate concentration in astrocytes; LAC_n, lactate concentration in neurons; O_{2c}, oxygen concentration in capillaries; O_{2T}, oxygen concentration in astrocytes and neurons; Cr_g, creatine concentration in astrocytes; Cr_n, creatine concentration in neurons; PCr_g, creatine phosphate concentration in astrocytes; PCr_n, creatine phosphate concentration in neurons; Na $PUMP_g$, glial Na/K-ATPase; Na $PUMP_n$, neuronal Na/K-ATPase; ATP_g, ATP concentration in astrocytes; ADP_g, ADP concentration in astrocytes; ATP_n, ATP concentration in neurons; ADP_n, ADP concentration in neurons; $NADH_g$, nicotinamide adenine dinucleotide (reduced form) concentration in astrocytes; $NADH_n$, nicotinamide adenine dinucleotide (reduced form) concentration in neurons; NAD^+_g, nicotinamide adenine dinucleotide (oxidized form) concentration in astrocytes; NAD^+_n, nicotinamide adenine dinucleotide (oxidized form) concentration in neurons; Na^+_e, extracellular Na^+ concentration; Na^+_g, Na^+ concentration in astrocytes; and Na^+_n, Na^+ concentration in neurons (adapted from [65]).

a decrease in the intracellular pH, force glioma cells from their viability domain, i.e., can kill them.

The model of basal physiological interaction of quiescent neurons and astrocytes was constructed by Cakir et al. [70]. This model describes the central metabolism (glycolysis, pentose phosphate pathway, and tricarboxylic acid cycle), oxidative phosphorylation, lipid metabolism, neutralization of reactive oxygen species, amino-acid metabolism, metabolism of neurotransmitters (dopamine, acetylcholine, norepinephrine, epinephrine, and serotonin), and metabolism between astrocytes and neurons (glutamate/glutamine cycle, serine/glycine cycle, etc.) in both cell types. The model contains 184 reactions in neurons and astrocytes, 33 intercellular metabolic processes, and 216 metabolites. The lactate transport from astrocyte to neuron (ANLS) was not taken into account based on the assumption that all reactions occur in quiescence. The scheme of the process considered in this model is shown in Fig. 12.

The use of this model for computing the distribution of metabolite flows between quiescent neurons and astrocytes agreed well with the published experimental data [71, 72]. The model was also applied to examine the dynamics of metabolite flows in hypoxia, i.e., under conditions of a gradual decrease in oxygen supply to cells. It is known that many brain diseases are associated with neurovascular disorders caused by an oxygen deficiency. A decrease in the cerebral blood supply leads to hypoxic regions in the brain, which substantially interfere with the brain's electric activity (for example, in epilepsy) or lead to progressive disease, such as dementia, Alzheimer's disease, and emotional disorders. In particular, the model demon-

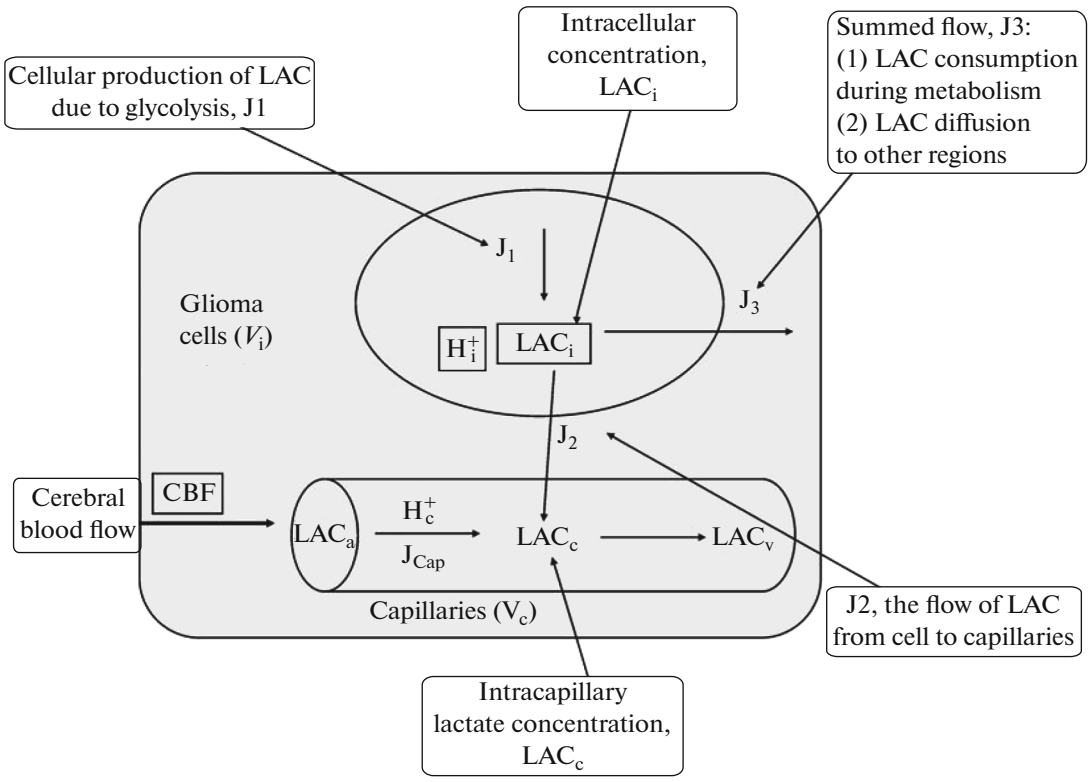

Fig. 11. The scheme of the processes considered in the model of hemodynamics and lactate metabolism in low-grade gliomas [67–69]: H_i^+ is the concentration of protons in cells; LAC_i, intracellular lactate concentration; LAC_c, intracapillary lactate concentration; LAC_a, lactate concentration in arteries; and LAC_v, lactate concentration in veins (adapted from [67]).

strated that a decrease in the oxygen flow to neurons (hypoxic conditions) leads to a drastic growth in the glucose influx there; this also fits the corresponding experimental data [73, 74]. An increase in the rate of glucose uptake by neurons in hypoxia is also a mechanism for combating the progression of Alzheimer disease [75].

CONCLUSIONS

Integration of mathematical models that describe specific biological and pathophysiological processes is a powerful tool for gaining insight into the complex molecular mechanisms that underlie the development of complex phenotypic traits and various diseases. It is expectable that elaboration of approaches to modeling the intricate biological systems will utilize the integration of simpler models that describe their components. Construction of integrated models for various specific features in the functioning of complex systems, such as calcium homeostasis in the body, virus–host interactions, and the human brain is the first step in this area. Such models have made it possible to study new mechanisms and conditions causing progression of various severe diseases, including musculoskeletal disorders and HCV infection at the levels of both intracellular processes and interaction of the virus with hepatocytes as well as various disorders in the brain function. The use of integrated models has enhanced the identification of the key targets and conditions for the directed effects of a new generation drugs, as well as interpretation of the results of state-of-the-art tomography technologies for examination of the brain in various pathologies. However, when integrating mathematical models, researchers inevitably encounter the problem of the description of the molecular mechanisms that underlie the interactions of biological processes, which makes the models considerably more complex and requires determination of manifold new parameters. The currently available data on the interactions between biological macromolecules are, as a rule, of an indirect character. Numerous as-yet-unknown mediators can be potentially involved in such interactions. Even when all players in the interactions are known, it is still difficult to experimentally determine the reaction rate constants and permissible ranges of their values. All these problems together make a challenge for mathematical biologists involved in construction of integrated models. One of the promising directions to solve the problem of a decrease in the number of estimated parameters that emerge when integrating models is the variant of

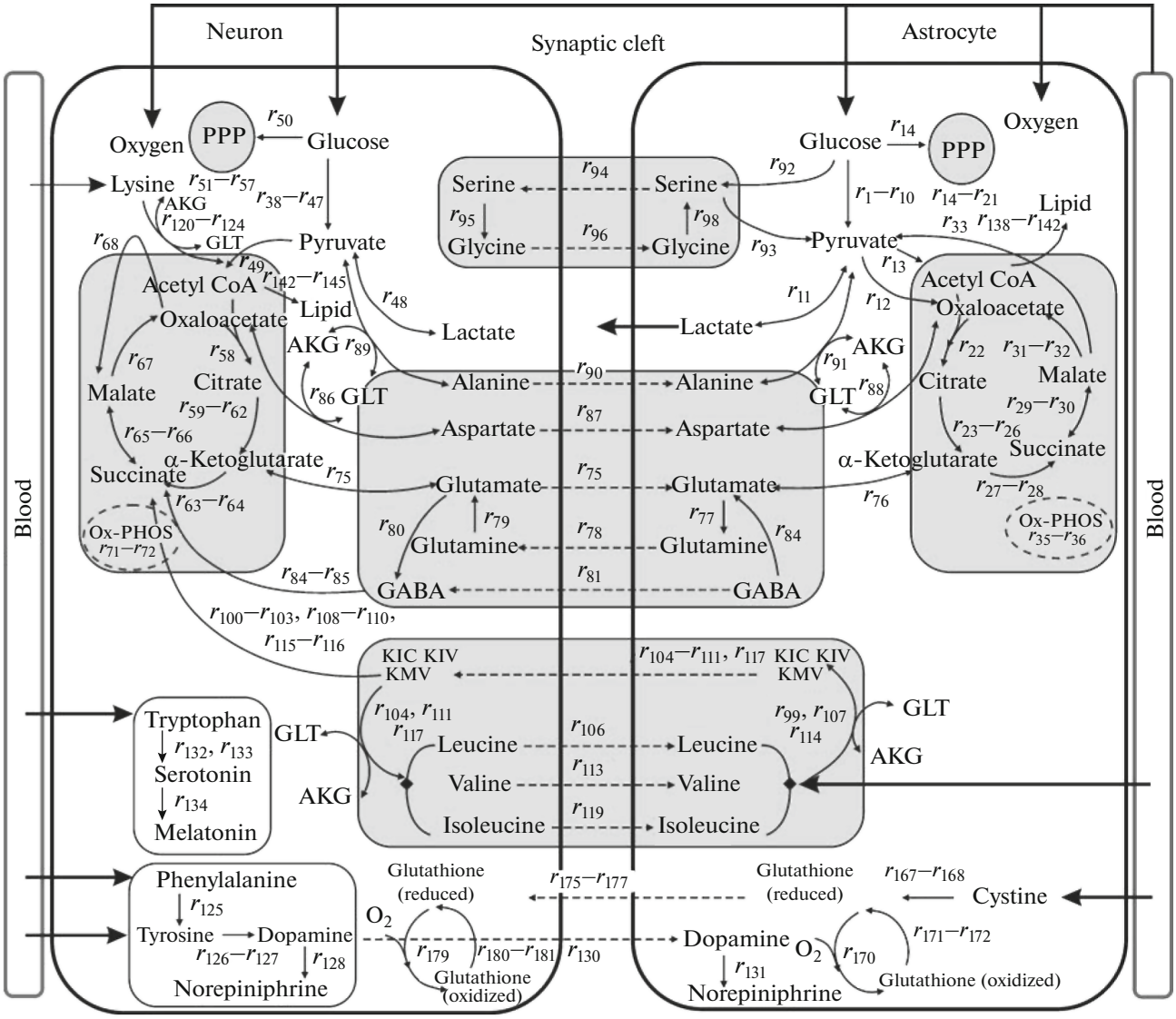

Fig. 12. The scheme of the main metabolic and exchange processes in the interaction of quiescent neurons and astrocytes considered in the model by Cakir et al. [70]: arrows denote the reactions of uptake and removal of metabolites; dashed arrows denote exchange transport of metabolites between cells of two types. For simplicity, only the main flows are shown (adapted from [70]).

mosaic gene-network models that utilize a control functional. This approach to integration based on the control function, first, does not require the addition of numerous new parameters; second, the corresponding parameters are assessable using abundant transcriptome experimental data on the changes in gene expression in a gene network in the case of gene knockout/knockdown in another gene network involved in a complex biological process.

ACKNOWLEDGMENTS

This work was supported by the Russian Science Foundation (project no. 14-44-00011 Programmed cell death induced via death receptors: identification of molecular mechanisms initiating apoptosis with the use of molecular modeling).

REFERENCES

1. C. K. Osborne, J. Shou, S. Massarweh, et al., Clin. Cancer Res. **11**, 865s (2005).
2. D. Javelaud and A. Mauviel, Oncogene **24**, 5742 (2005).
3. J. Hiscott, H. Kwon, and P. Génin, J. Clin. Invest. **107**, 143 (2001).
4. M. T. Mc Auley, D. J. Wilkinson, J. J. Jones, et al., BMC Syst. Biol. **6**, 130 (2012).
5. M. Fribourg, B. Hartmann, M. Schmolke, et al., J. Theor. Biol. **351**, 47 (2014).

6. N. V. Ivanisenko, E. L. Mishchenko, I. R. Akberdin, et al., PLOS ONE **9**, e91502 (2014).
7. M. Baker, S. Denman-Johnson, B. S. Brook, et al., Math. Med. Biol. **30**, 311 (2013).
8. M. Krupp, J. U. Marquardt, U. Sahin, et al., Bioinformatics **28**, 1184 (2012).
9. R. Leinonen, H. Sugawara, and M. Shumway, Nucleic Acids Res. **39**, D19 (2011).
10. O. V. Popik, E. D. Petrovskiy, E. L. Mishchenko, et al., Virus Res. **218**, 71 (2016).
11. G. Jones, S. A. Strugnell, and H. F. DeLuca, Physiol. Rev. **78**, 1193 (1998).
12. J. F. Raposo, L. G. Sobrinho, and H. G. Ferreira, J. Clin. Endocrinol. Metab. **87**, 4330 (2002).
13. V. Lemaire, F. L. Tobin, L. D. Greller, et al., J. Theor. Biol. **229**, 293 (2004).
14. S. Pozzi, M. Fulciniti, H. Yan, et al., Bone **53**(2), 487 (2013).
15. A. A. Ali., R. S. Weinstein, S. A. Stewart, et al., Endocrinology **146**(3), 1226 (2005).
16. M. C. Peterson and M. M. Riggs, Bone **46**, 49 (2010).
17. T. Bellido, A. A. Ali, L. I. Plotkin, et al., J. Biol. Chem. **278**, 50259 (2003).
18. M. R. McClung, E. M. Lewiecki, S. B. Cohen, et al., N. Engl. J. Med. **354**, 821 (2006).
19. P. Chen, J. H. Satterwhite, A. A. Licata, et al., J. Bone Miner. Res. **20**, 962 (2005).
20. D. M. Slovik, R. M. Neer, and J. T. Potts, J. Clin. Invest. **68**, 1261 (1981).
21. S. J. Silverberg, E. Shane, T. P. Jacobs, et al., N. Engl. J. Med. **341**, 1249 (1999).
22. M. Rix, H. Andreassen, P. Eskildsen, et al., Kidney Int. **56**, 1084 (1999).
23. K. Kruse, U. Kracht, K. Wohlfart, et al., Eur. J. Pediatr. **148**, 535 (1989).
24. J. P. Messina, I. Humphreys, A. Flaxman, et al., Hepatology **61**, 77 (2015).
25. J. F. Perz, G. L. Armstrong, L. A. Farrington, et al., J. Hepatol. **45**, 529 (2006).
26. A. U. Neumann, N. P. Lam, H. Dahari, et al., Science **282**, 103 (1998).
27. H. Dahari, A. Lo, R. M. Ribeiro, et al., J. Theor. Biol. **247**, 371 (2007).
28. H. Dahari, R. M. Ribeiro, and A. S. Perelson, Hepatology **46**, 16 (2007).
29. L. Rong, H. Dahari, R. M. Ribeiro, et al., Sci. Transl. Med. **2**, 30ra32 (2010).
30. J. Guedj and A. S. Perelson, Hepatology **53**, 1801 (2011).
31. B. S. Adiwijaya, E. Herrmann, B. Hare, et al., PLoS Comput. Biol. **6**, e1000745 (2010).
32. B. S. Adiwijaya, T. L. Kieffer, J. Henshaw, et al., PLoS Comput. Biol. **8**, e1002339 (2012).
33. H. Dahari, R. M. Ribeiro, C. M. Rice, et al., J. Virol. **81**, 750 (2007).
34. M. Binder, N. Sulaimanov, D. Clausznitzer, et al., PLoS Pathog. **9**, e1003561 (2013).
35. E. L. Mishchenko, K. D. Bezmaternykh, V. A. Likhoshvai, et al., J. Bioinform. Comput. Biol. **5**, 593 (2007).
36. C. Laouénan, P. Marcellin, M. Lapalus, et al., Antimicrob. Agents Ch. **58**, 5332 (2014).
37. B. Roche, A. Coilly, A. M. Roque-Afonso, et al., Viruses **7**, 5155 (2015).
38. V. Belousova, A. A. Abd-Rabou, and S. A. Mousa, Pharmacol. Ther. **145**, 92 (2015).
39. B. S. Adiwijaya, B. Hare, P. R. Caron, et al., Antivir. Ther. **14**, 591 (2009).
40. H. W. Reesink, G. C. Fanning, and K. A. Farha, Gastroenterology **138**, 913 (2010).
41. M. Gao, R. E. Nettles, M. Belema, et al., Nature **465**, 96 (2010).
42. N. Forestier, D. Larrey, D. Guyader, et al., J. Hepatol. **54**, 1130 (2011).
43. J. de Bruijne, A. van Vliet, C. J. Weegink, et al., Antivir. Ther. **17**, 633 (2012).
44. J. Guedj and A. U. Neumann, J. Theor. Biol. **267**, 330 (2010).
45. J. Guedj, H. Dahari, L. Rong, et al., Proc. Natl. Acad. Sci. U. S. A. **110**, 3991 (2013).
46. L. Rong, J. Guedj, H. Dahari, et al., PLoS Comput. **9**, e1002959 (2013).
47. D. Clausznitzer, J. Harnisch, and L. Kaderali, Virus Res. **218**, 96 (2016).
48. N. David, Y. Yaffe, L. Hagoel, et al., Virology **475**, 139 (2015).
49. N. Appel, M. Zayas, S. Miller, et al., PLoS Pathog. **4**, e1000035 (2008).
50. S. Yamauchi, K. Takeuchi, K. Chihara, et al., J. Biol. Chem. **290**, 21857 (2015).
51. M. Schliemann, E. Bullinger, S. Borchers, et al., BMC Syst. Biol. **5**, 204 (2011).
52. N. Papic, C. I. Maxwell, D. A. Delker, et al., Viruses **4**, 581 (2012).
53. N. Zhu, C. F. Ware, and M. M. Lai, Virology **283**, 178 (2001).
54. Y. M. Chung, K. J. Park, S. Y. Choi, et al., Biochem. Biophys. Res. Commun. **284**, 15 (2001).
55. A. Aubert, R. Costalat, and R. Valabrègue, Acta Biotheor. **49**, 301 (2001).
56. T. A. Rapoport and R. Heinrich, Biosystems **7**, 120 (1975).
57. R. Heinrich and S. Schuster, *The regulation of Cellular Systems* (Chapman & Hall, New York, 1996).
58. M. S. Vafaee and A. Gjedde, J. Cereb. Blood Flow Metab. **20**, 747 (2000).
59. A. Aubert and R. Costalat, Neuroimage **17**, 1162 (2002).
60. R. B. Buxton, E. C. Wong, and L. R. Frank, Magn. Reson. Med. **39**, 855 (1998).
61. J. Frahm, G. Krüger, K. D. Merboldt, et al., Magn. Reson. Med. **35**, 143 (1996).
62. G. Krüger, A. Kastrup, A. Takahashi, et al., Neuroreport **10**, 2939 (1999).
63. A. Toglia, J. M. Kittelson, R. B. Roemer, et al., Int. J. Hyperthermia **2**, 461 (1996).
64. A. Aubert, R. Costalat, H. Duffau, et al., Acta Biotheor. **50**, 281 (2002).

65. A. Aubert and R. Costalat. J. Cereb. Blood Flow Metab. **25**, 1476 (2005).
66. A. Aubert, R. Costalat, P. J. Magistretti, et al., Proc. Natl. Acad. Sci. U. S. A. **102**, 16448 (2005).
67. R. Guillevin, C. Menuel, J. N. Vallée, et al., Compt. Rend. Biol. **334**, 31 (2011).
68. R. Costalat, J. P. Francoise, C. Menuel, et al., Acta Biotheor. **60**, 99 (2012).
69. M. Lahutte-Auboin, R. Guillevin, J. P. Françoise, et al., Acta Biotheor. **61**, 79 (2013).
70. T. Cakir, S. Alsan, H. Saybaşili, et al., Theor. Biol. Med. Model. **4**, 48 (2007).
71. L. Hertz, Neurochem. Int. **45**, 285 (2004).
72. J. Shen, K. F. Petersen, K. L. Behar, et al., Proc. Natl. Acad. Sci. U. S. A. **96**, 8235 (1999).
73. L. R. Drewes and D. D. Gilboe, J. Biol. Chem. **248**, 2489 (1973).
74. S. I. Harik, R. A. Behmand, and J. C. LaManna, J. Appl. Physiol. **77**, 896 (1994).
75. N. J. Allen, R. Káradóttir, and D. Attwell, J. Neurosci. **25**, 848 (2005).

Translated by G. Chirikova